A distributed-absorber cold-electron bolometer single pixel at 95 GHz

S. Mahashabde,[1,a)] M. A. Tarasov,[2,1] M. Salatino,[1,3] A. Sobolev,[2,4] S. Masi,[3] L. S. Kuzmin,[1] and P. de Bernardis[3]
[1]*Chalmers University of Technology, Göteborg 41296, Sweden*
[2]*Kotel'nikov Institute of Radio Engineering and Electronics, 125009 Mokhovaya st 11/7, Moscow, Russia*
[3]*Physics Department, Sapienza University of Rome, p.le Aldo Moro, 2 00185 Rome, Italy*
[4]*Moscow Institute of Physics and Technology (State University), 141700 Institutsky per. 9, Dolgoprudny, Moscow, Russia*

(Received 30 March 2015; accepted 14 August 2015; published online 2 September 2015)

We describe a Frequency Selective Surface (FSS) based distributed-absorber Cold-Electron Bolometer (CEB) pixel at 95 GHz integrated in a multi-moded horn. The FSS provides a resonant interaction with incident mm and sub-mm radiation and defines the bandwidth of the array while the horn provides the matching of the beam to the telescope optics. CEB detectors with matched impedance are integrated within the periodic elements of the FSS and generate a voltage response proportional to the incident optical power in the bandwidth of the FSS. A prototype pixel was designed, fabricated, and characterized at a temperature of 280 mK. We present optical response to blackbody radiation and fit it to the CEB model. For an absorbed power of 50 pW, we estimate an optical responsivity of 1.2×10^8 V/W and a readout dominated Noise Equivalent Power (NEP) of 1.8×10^{-15} W Hz $^{-1/2}$. A measured bandwidth of 9 GHz of this detector array confirms the frequency selective nature. This prototype represents a possible solution as a detector for the 95 GHz channel of the SWIPE instrument on the LSPE balloon-borne telescope. This kind of FSS based mm-wave architecture can be easily scaled to other frequency ranges and used on any other balloon-borne telescope focal planes. © *2015 AIP Publishing LLC*.
[http://dx.doi.org/10.1063/1.4929604]

The measurement of the polarized component of the Cosmic Microwave Background (CMB) is the main target of several astrophysical experiments observing the sky in the sub-millimeter/far-infrared regime like ACTPol,[1] EBeX,[2] LSPE,[3] and SPIDER.[4] This interest comes from the fact that the CMB is a powerful probe for understanding if an inflationary process really occurred during the Planck era. The CMB can also be used for studying several astrophysical observables[5] such as galaxy clusters, dark matter, and neutrino masses through Sunyaev-Zel'dovich (SZ) effect.[6] The recent BICEP2 and Planck joint analysis[7] demonstrated the compelling necessity of performing polarization measurements of the CMB foregrounds in the frequency bands where the astrophysical emissions dominate over the cosmological signal. The demanding need of detecting these tiny polarized signals, i.e., of the order of fractions of μK, with photon-noise limited detectors drives the development of large focal plane arrays able to accommodate thousands of single-mode detectors,[6] or alternatively hundreds of multi-moded detectors.[8,9] The multi-mode solution is appealing when high angular resolution is not the driver of the measurement, as in the case of measurements of B-modes in the CMB polarization. In this case, a moderate-sized array of multi-moded detectors can collect the same number of modes as a much larger array of single-mode detectors. For photon-noise limited measurements, the survey sensitivity depends on the total number of modes collected by the array, so the same survey sensitivity is obtained with a smaller number of detectors in the case of multi-moded detectors, resulting in a significant simplification of the instrument. In low-background applications, the Noise Equivalent Power (NEP) of multi-moded detectors is dominated by photon-noise while the NEP of single-mode detectors can have a significant additional contribution from intrinsic detector noise. This means that the same final survey sensitivity of a focal plane filled with single-moded detectors can be obtained with a multi-moded detector filled focal plane operating at a higher temperature (300 mK instead of 100 mK), further simplifying the instrument. In addition, we use the CEB as the detector in this work. The CEB technology is attractive from the point of view of the low sensitivity of the detectors to cosmic rays[10] due to its very small cross section. The CEB also has a high dynamic range and its sensitivity decreases gradually as it absorbs increasing amounts of power.[11] This is important considering the fluctuating atmospheric background power loads on balloon-borne telescopes. The fabrication of the device is also reliable and avoids the use of thin membranes. Due to these attractive properties, we believe that the prototype pixel described in this paper can be a good candidate for balloon-borne experiments. We report the design and characterization of a single prototype pixel for the 95 GHz channel on the SWIPE[12] instrument which is the short wavelength polarimeter of the Large Scale Polarization Explorer (LSPE).[3]

FSS have been well studied and utilized in design of frequency selective bolometers[13] with a Transition Edge Sensor fabricated on a thin membrane.[14] The FSS is a periodic arrangement of repeated metallic elements. Each element has an inductance and a mutual capacitance that exists between neighboring elements. A well designed periodic

[a)]Electronic mail: sumedh@chalmers.se

array can resonate with incident electromagnetic radiation at the frequency of interest. If a detector like a CEB[15] is inserted in such an element, then high frequency currents excited due to the incident radiation can be coupled to the detector, creating an optical response.

The pixels on the focal plane of a balloon-borne telescope typically have a large atmospheric power load incident on them, up to a level of tens of picowatts. A single CEB detector can handle a finite amount of power before its responsivity is reduced, so an array of CEBs is required to handle the large background power. The detectors need to be integrated in a structure which can uniformly distribute the background power over all the CEBs. The CEB integrated FSS also works as a band defining filter and, in principle, can substitute a traditional metal mesh bandpass filter, which has been known to introduce an extra background power load due to inefficient cooling of the metal mesh.[16] We believe that integrating CEBs in a FSS can be useful in decreasing losses associated with a separate bandpass filter. This approach is similar to the frequency selective bolometers, and we can expect similar bandwidths for well designed pixels as previously reported.[13,14]

The unit cell of the prototype pixel used in this study is a circular metallic shape with orthogonal slots containing 4 CEBs on a silicon substrate shunted with a backshort. A schematic of the unit cell drawn in the commercial 3D electromagnetic simulation package HFSS is shown in Fig. 1(a). The unit cell is simulated by illuminating it with two orthogonal polarizations of a plane wave. Periodic boundary conditions are assigned to simulate an array. Initial values of various physical dimensions can be estimated using the one dimensional transmission line model described in Ref. 17. The silicon substrate thickness and the backshort distance act as a piece of transmission line shunting the periodic FSS structure. By varying the thickness of the substrate and unit cell pitch, the structure is brought to resonance at the frequency of interest (95 GHz). The embedded CEB detectors are also simulated in the HFSS design using lumped elements whose properties correspond to typical CEB resistance and capacitance. A fractional bandwidth of about 10% has been achieved in RF simulations and efforts are ongoing to increase this bandwidth.

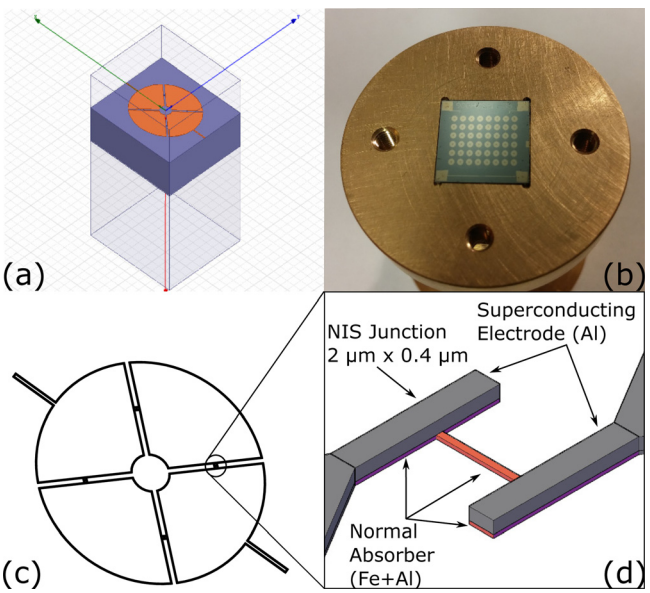

FIG. 1. (a) Unit cell design in HFSS. The unit cell pitch is 1055 μm. (b) Optical image of the pixel mounted in the sample holder. The chip dimension is 11 mm × 11 mm. The central 6 × 6 unit cells are connected in series forming the pixel. Each element contains 4 CEBs, 2 in series and 2 in parallel. (c) A schematic of the FSS element with 4 bolometers integrated in the orthogonal slots. (d) Details of a single CEB. The resistive strip is 1.5 μm in length and 100 nm in width. The normal metal is oxidized and extends below the superconductor to form the NIS junction.

The CEB array embedded in the FSS consists of N bolometers in series and W in parallel from a DC point of view (144 bolometers—72 in series and 2 in parallel in this case). P_0 is the background power on the pixel in steady state while δP is the incident signal power. The incident power and the bias current heat up the electron system of the absorber while the tunneling of electrons with energies larger than the Fermi energy of the normal metal across the NIS junction leads to cooling of the electron system. There also exists a heating factor corresponding to the direct Joule heating of the absorber due to the resistance of the absorber R_a and the bias current I. The heating processes lead to an increase of electron temperature and the cooling processes decrease it. The heat balance can be described as

$$2P_N + 2\beta P_S - \Sigma\Lambda\left(T_e^5 - T_{ph}^5\right) + I^2R_a + \frac{P_0 + \delta P}{N \times W} = 0. \quad (1)$$

Here, P_N is the power transferred to the normal metal by the bias current. The value of P_N is negative due to electron cooling. P_S is the power deposited in the superconducting electrode. P_N and P_S are described in Refs. 18 and 19. The parameter β accounts for the amount of power returning back from the superconducting electrodes to the normal absorber.[20] The factor 2 arises due to the two NIS junctions in the CEB. $\Sigma\Lambda(T_e^5 - T_{ph}^5)$ is the heat lost by the electron system to the phonon system in the absorber, Σ is the electron-phonon coupling constant ($1.1 \times 10^9\,\mathrm{Wm^{-3}K^{-5}}$), which is material and temperature dependent, Λ is the volume of the normal absorber, and T_e and T_{ph} are its electron and phonon temperatures, respectively.

The response of the bolometric array to the incident power depends on the electron temperature of the absorber and the absorbed power. Due to the nonlinear nature of the NIS IV characteristics, the responsivity is different along different points on the IV curve. This responsivity can be estimated using the expression[21]

$$S_V = \frac{\delta V}{\delta P}. \quad (2)$$

The CEB is a multilayer structure consisting of a non-superconducting absorber, a tunnel barrier, and two superconducting electrodes. The normal metal absorber is a bilayer of 0.7 nm iron and 12 nm aluminum. It is patterned in the shape of the NIS junctions with dimensions 2 μm × 0.4 μm and separated by a thin resistive strip of size 1.5 μm × 100 nm as shown in Fig. 1(d). The total volume of the normal absorber is about 0.023 μm^3. The normal metal is then oxidized, and the superconducting electrode is deposited on top. Shadow evaporation ensures that the superconducting aluminum is deposited only on the NIS junction area and not on the thin resistive

strip. The normal state resistance of each NIS junction is 400 Ω, and the resistance of absorbing strip is 80 Ω. The subgap impedance of the full pixel at the point of maximum responsivity (Fig. 4(c)) is 2.5 MΩ, which is compatible with the noise impedance of cold JFET amplifiers,[22] assuming a current noise spectral density of 1–2 fA Hz $^{-1/2}$. The subgap impedance can be easily tuned by changing the normal state resistance of the NIS junctions during fabrication.

The fabricated sample has an array of 8×6 unit cells of which the central 6×6 cells form the pixel and the rest are used as test structures. The chip dimension is 11 mm × 11 mm, while the pixel dimension is 6.3 mm × 6.3 mm. The total active area of the bolometers on the chip is about 300 μm^2, which is extremely small compared to other recently described multimode detectors.[9] This can help to decrease the influence of Cosmic Ray hits (spikes) on the measured signal. The outer diameter of the FSS ring shown in Fig. 1(c) is 745 μm, and the diameter of the inner circle is 123 μm. The device is fabricated on a high resistivity (>2 kΩ cm) intrinsically doped silicon substrate of thickness 320 μm. A backshort is placed at a distance of 350 μm from the pixel. Alignment marks, FSS elements, and contact pads are fabricated in 300 nm thick gold to decrease RF losses.

We characterized the spectral response of the sample by illuminating it with a Backward Wave Oscillator (BWO). The measurement schematic is shown in Fig. 2(a). The sample was cooled down to 280 mK in a testbed cryostat. A multimode horn[8] provided optical coupling to incident radiation, while a filter chain (a pair of fluorogold filters and a pair of custom neutral density filters mounted on the 2.7 K stage of the cryostat) attenuated the thermal radiation from the 300 K background. Problematic reflections from cryostat shields

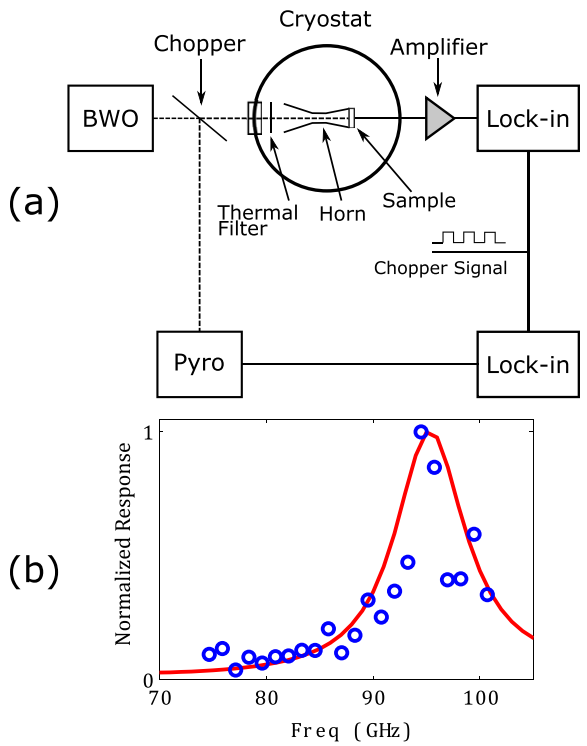

FIG. 2. (a) Spectral response measurement setup. (b) Measured spectral response (open circles) compared with the simulation from HFSS package (solid line).

were minimized by the use of RF absorbing foam. Using a chopper tilted 45° with respect to the normal axis of the BWO, the incident radiation was alternatively transmitted to the sample or reflected towards a pyroelectric detector. The spectral response of the sample was synchronously demodulated and normalized against the pyroelectric detector's response and compared with RF simulations in Fig. 2(b). The deviation of the experimental data from the simulation is most likely due to the residual reflections between cryostat shields.

With mm-wave radiation emitted from a custom blackbody mounted on the 2.7 K stage of our testbed cryostat as shown in Fig. 3, we characterized the optical response of the sample. Given the volume constraints inside the cryostat, the multi-moded horn was substituted by a smaller one without the backwards flare. In order to decrease the background radiation, the horn aperture was reduced to a circle of diameter 5 mm. The blackbody source was heated in the temperature range of 2.7–4.2 K, and the current-voltage (IV) curves of the pixel were recorded as a function of the blackbody temperature. Planck's law was used to estimate the incident power, while the absorbed power was estimated from the CEB model described earlier.

Using Eq. (1), we have fitted the measured IV characteristics to the CEB model. The estimated background power inside the cryostat was 47.2 pW. The value of the absorbed power for each IV curve was extracted from the data fits, and these power levels are shown in Fig. 4(a) after subtracting the background power on the device. Responsivity of the device estimated using data fitting is shown in Fig. 4(b), and it approaches 1.2×10^8 V/W for 50 pW absorbed power. The value of responsivity reported for a single CEB with a titanium absorber in Ref. 23 is very similar to the current work with a proportionally lower absorbed power. In comparison, the reported responsivity of a semiconductor CEB[24] is lower

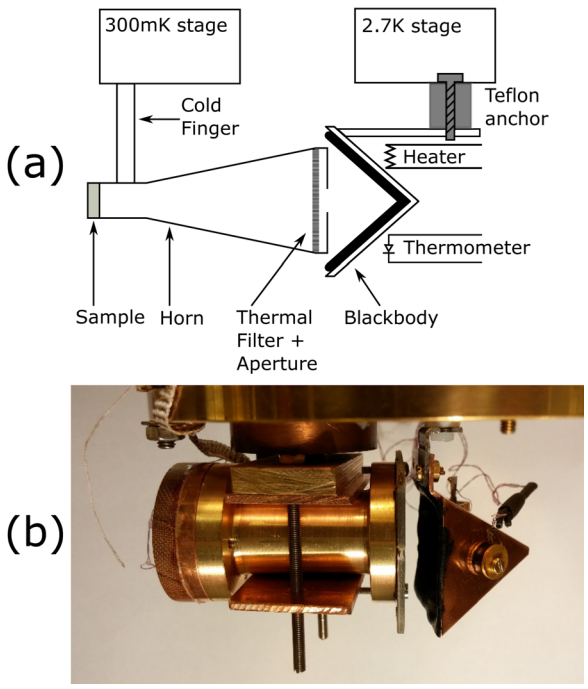

FIG. 3. (a) Cold optical response measurement setup. (b) A photograph of the blackbody and the horn used for measurements.

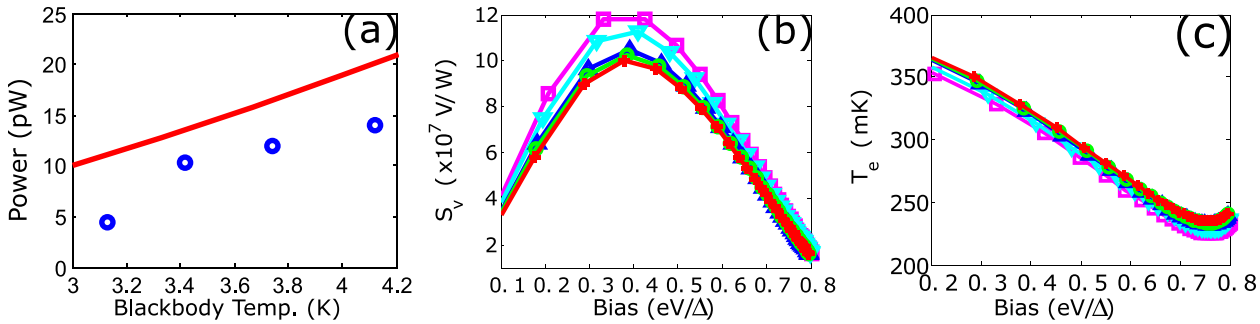

FIG. 4. (a) Plot of estimated absorbed power (open circles) plotted against incident power (solid line) on the device. Background power on the device has been subtracted. (b) The estimated responsivity from data analysis in dependence on absorbed power. (c) Electron temperature of the CEB absorber as a function of voltage bias at various blackbody temperatures. The electron temperature is estimated using Eq. (1). The blackbody temperatures and the corresponding absorbed powers including the background shown in (b) and (c) are: 2.6 K and 47.2 pW (squares), 3.13 K and 51.6 pW (inverted triangles), 3.42 K and 57.5 pW (triangles), 3.74 K and 59.2 pW (circles), and 4.12 K and 61.1 pW (stars).

by an order of magnitude than the current work. The extracted electron temperature of the CEB absorbers at various absorbed powers are shown in Fig. 4(c) demonstrating electron cooling, which is a fundamental property of the CEB.

Using the noise model of the CEB,[21] we can estimate the contributions of the noise due to the NIS junctions and the noise due to electron-phonon coupling to the device NEP. The estimated NEP due to NIS tunneling is 1.5×10^{-16} W Hz$^{-1/2}$, and the NEP due to electron−phonon coupling is 3.5×10^{-17} W Hz $^{-1/2}$. The photon NEP can be approximated as $\sqrt{2P_0 h\nu + 2P_0^2/\delta\nu}$ and is estimated to be 7.5×10^{-16} W Hz $^{-1/2}$. Here, h is the Planck constant, ν is the frequency at the centre of the optical band, $\delta\nu$ is the optical bandwidth (9 GHz), and $P_0 = 50$ pW.

Using room temperature commercial JFET amplifiers (AD743), we have recorded a NEP of 1.8×10^{-15} W Hz $^{-1/2}$, which is about 2.5 times higher than the photon NEP at a power load of 50 pW. The voltage noise[22] from a JFET cooled to 120 K is about 4×10^{-9} V Hz $^{-1/2}$. Using a cooled JFET amplifier as the first stage of the readout of this pixel can bring a readout limited NEP of 4×10^{-17} W Hz $^{-1/2}$ using the responsivity values from Fig. 4(c). A more innovative readout[24] has been recently reported and can in theory lower the readout NEP to 2.5×10^{-18} W Hz $^{-1/2}$.

We have developed and characterized a prototype 95 GHz planar bolometric single pixel with the Cold-Electron bolometers. The spectral measurements confirm the frequency selective characteristics of the pixel with an estimated bandwidth of 9 GHz. Optical sensitivity is demonstrated using a blackbody source, and resulting data fits indicate a strong optical response with an estimated responsivity of 1.2×10^8 V/W for 50 pW absorbed power. This sensitivity is adequate for balloon-borne missions and the impedance of the detectors is compatible with a cold JFET readout.

[1]M. Niemack, P. Ade, J. Aguirre, F. Barrientos, J. Beall, J. Bond, J. Britton, H. Cho, S. Das, M. Devlin *et al.*, Proc. SPIE **7741**, 77411S (2010).
[2]B. Reichborn-Kjennerud, A. M. Aboobaker, P. Ade, F. Aubin, C. Baccigalupi, C. Bao, J. Borrill, C. Cantalupo, D. Chapman, J. Didier *et al.*, Proc. SPIE **7741**, 77411C–77411C (2010).
[3]S. Aiola, G. Amico, P. Battaglia, E. Battistelli, A. Baù, P. de Bernardis, M. Bersanelli, A. Boscaleri, F. Cavaliere, A. Coppolecchia *et al.*, "Ground-based and airborne instrumentation for astronomy IV," Proc. SPIE **8446**, 84467A–84467A (2012).
[4]A. Rahlin, P. Ade, M. Amiri, S. Benton, J. Bock, J. Bond, S. Bryan, H. C. Chiang, C. Contaldi, B. Crill *et al.*, Proc. SPIE **9153**, 915313–915313 (2014).
[5]K. Abazajian, K. Arnold, J. Austermann, B. Benson, C. Bischoff, J. Bock, J. Bond, J. Borrill, I. Buder, D. Burke *et al.*, Astropart. Phys. **63**, 55 (2015).
[6]K. N. Abazajian, K. Arnold, J. Austermann, B. Benson, C. Bischoff, J. Bock, J. Bond, J. Borrill, E. Calabrese, J. Carlstrom *et al.*, Astropart. Phys. **63**, 66 (2015).
[7]P. Ade *et al.*, Phys. Rev. Lett. **114**, 101301 (2015).
[8]L. Lamagna, D. Bagliani, M. Biasotti, P. de Bernardis, F. Gatti, R. Gualtieri, S. Masi, and G. Pisano, in *International Conference on Electromagnetics in Advanced Applications (ICEAA)* (IEEE, 2013), pp. 1201–1204.
[9]M. Biasotti, D. Bagliani, D. Corsini, V. Ceriale, P. de Bernardis, F. Gatti, R. Gualtieri, L. Lamagna, S. Masi, G. Pizzigoni *et al.*, Proc. SPIE **9153**, 915308 (2014).
[10]M. Salatino, P. de Bernardis, L. Kuzmin, S. Mahashabde, and S. Masi, J. Low Temp. Phys. **176**, 323–330 (2014).
[11]L. Kuzmin, "Millimeter and submillimeter detectors for astronomy II," Proc. SPIE **5498**, 349 (2004).
[12]P. de Bernardis, S. Aiola, G. Amico, E. Battistelli, A. Coppolecchia, A. Cruciani, A. D'Addabbo, G. D'Alessandro, S. De Gregori, M. De Petris *et al.*, "Millimeter, submillimeter, and far-infrared detectors and instrumentation for astronomy VI," Proc. SPIE **8452**, 84523F (2012).
[13]M. Kowitt, D. Fixsen, A. Goldin, and S. Meyer, Appl. Opt. **35**, 5630 (1996).
[14]D. W. Logan, "A frequency selective bolometer camera for measuring millimeter spectral energy distributions," Ph.D. thesis (University of Massachusetts, Amherst, 2009).
[15]L. Kuzmin, in *International Workshop on Superconducting Nano-Electronics Devices* (Springer, 2002).
[16]J. Bueno, P. de Visser, S. Doyle, and J. Baselmans, J. Low Temp. Phys. **176**, 1089–11095 (2014).
[17]S. Mahashabde, A. S. Sobolev, M. A. Tarasov, G. E. Tsydynzhapov, and L. S. Kuzmin, IEEE Trans. Terahertz Sci. Technol. **5**, 37 (2014).
[18]G. O'Neil, "Improving NIS tunnel junction refrigerators— Modeling, materials, and traps," Ph.D. thesis (University of Colorado at Boulder, 2011).
[19]S. Mahashabde, A. Sobolev, A. Bengtsson, D. Andrén, M. A. Tarasov, M. Salatino, P. de Bernardis, S. Masi, and L. S. Kuzmin, IEEE Trans. Terahertz Sci. Technol. **5**, 145 (2014).
[20]P. Fisher, J. Ullom, and M. Nahum, Appl. Phys. Lett. **74**, 2705 (1999).
[21]D. Golubev and L. Kuzmin, J. Appl. Phys. **89**, 6464 (2001).
[22]A. Alessandrello, C. Brofferio, O. Cremonesi, A. Giuliani, M. Pedretti, A. Nucciotti, M. Pavan, G. Pessina, and E. Previtali, IEEE Trans. Nucl. Sci. **47**, 1851 (2000).
[23]E. Otto, M. Tarasov, P. K. Grimes, A. Chekushkin, L. S. Kuzmin, and G. Yassin, Supercond. Sci. Technol. **26**, 085020 (2013).
[24]T. Brien, P. Ade, P. Barry, C. Dunscombe, D. Leadley, D. Morozov, M. Myronov, E. Parker, M. Prest, M. Prunnila *et al.*, Appl. Phys. Lett. **105**, 043509 (2014).